small
Nanotube Arrays

Hierarchical MoS_2 Nanosheet@TiO_2 Nanotube Array Composites with Enhanced Photocatalytic and Photocurrent Performances

*Lingxia Zheng, Sancan Han, Hui Liu, Pingping Yu, and Xiaosheng Fang**

A novel type of hierarchical nanocomposites consisted of MoS_2 nanosheet coating on the self-ordered TiO_2 nanotube arrays is successfully prepared by a facile combination of anodization and hydrothermal methods. The MoS_2 nanosheets are uniformly decorated on the tube top surface and the intertubular voids with film appearance changing from brown to black color. Anatase TiO_2 nanotube arrays (NTAs) with clean top surfaces and the appropriate amount of MoS_2 precursors are key to the growth of perfect compositing TiO_2@MoS_2 hybrids with significantly enhanced photocatalytic activity and photocurrent response. These results reveal that the strategy provides a flexible and straightforward route for design and preparation nanocomposites based on functional semiconducting nanostructures with 1D self-ordered TiO_2 NTAs, promising for new opportunities in energy/environment applications, including photocatalysts and other photovoltaic devices.

1. Introduction

Since the pioneering work on water splitting by Fujishima and Honda,[1] titanium dioxide (TiO_2) has been extensively investigated and remained as one of the most promising candidates for photocatalysts and photoelectrodes due to its high chemical stability, favorable band edge positions, strong optical absorption, eco-friendliness, and abundant availability.[2–5] Among different crystal structures and morphologies of TiO_2, vertically oriented anatase 1D TiO_2 nanotube arrays (TiO_2 NTAs) grown by a simple electrochemical anodization method show the highest activity for solar energy conversion in the viewpoint of high surface-to-volume ratio and excellent electron transport property.[6–8] More importantly, the structural characteristics (tube diameters, length, tube packing densities, etc.) of TiO_2 NTAs can be facilely controlled by fine design of anodization process (such as anodization time, potential/current, electrolyte, and temperature).[4,9,10] However, as an n-type wide band gap semiconductor, TiO_2 can solely absorb the UV light, which accounts for less than 5% over the full solar resource, thus significantly limiting its widespread applications. In addition, the rapid recombination rate of photogenerated electron-hole pairs of TiO_2 leads to a low quantum efficiency and poor photocatalytic activity. In order to address these obstacles, a plethora of strategies have been explored to improve the photoresponse of 1D TiO_2 NTAs. For example, metal/nonmetal impurity doping was shown to introduce mid-gap energy levels, which were expected to control the band gap response of the TiO_2 NTAs and enhance their visible spectrum properties.[11–15] In particular, the growth of TiO_2-based composites (core-shell geometry or nanoparticle decoration) is considered to be one of the most promising routes due to the improvement of charge carrier separation.[16–19] It is of paramount importance to design efficient semiconductor-based composites with desirable architectural structure/morphology enabling synergistic impacts on the overall performance of photocatalytic and photoelectrochemical applications.

Molybdenum disulfide (MoS_2), a member of the layered transition metal dichalcogenides family, has been a focus of study for wide applications due to its high activity, excellent morphologies, good electronic and optical properties, such

Dr. L. X. Zheng, S. C. Han, Dr. H. Liu, Dr. P. P. Yu, Prof. X. S. Fang
Department of Materials Science
Fudan University
Shanghai 200433, P. R. China
E-mail: xshfang@fudan.edu.cn

DOI: 10.1002/smll.201503441

© 2016 Wiley-VCH Verlag GmbH & Co. KGaA, Weinheim

as supercapacitors, hydrogen storage, catalysis, microelectronics, and optoelectronic.[20–27] With an analog structure to graphene, each layer of MoS_2 consists of molybdenum atoms sandwiched between two layers of hexagonally close-packed sulfur atoms and the sandwiched adjacent layers are held together by the weak van der Waals forces. To date, the MoS_2-based semiconductor heterostructures, such as CdS/MoS_2,[28] MoO_3/MoS_2,[29] SnO_2/MoS_2,[30] with good photocatalytic or photoelectrochemical properties have been successfully synthesized, since the efficient charge separation can be obtained by coupling two semiconductor structures with the matched energy levels. In particular, MoS_2/TiO_2 nanocomposites are one of the best candidates for contributing to superior energy and environment performances given their great crystal-modification potential for conductance, aspect ratio, and ultrathin edges. There are a few existing studies of MoS_2/TiO_2 nanocomposites with remarkable photocatalytic activity or lithium storage performances.[27,31–38] For example, Zhang et al.[27] reported a 3D hierarchical heterostructures constructed by few-layer MoS_2 nanosheet coating on the TiO_2 nanobelts with enhanced photocatalytic efficiency. Xu et al.[39] demonstrated that the MoS_2 nanosheet@TiO_2 nanotube hybrids prepared via a template-assisted hydrothermal method exhibited high reversible lithium storage capacity and superior rate capability. However, the reported MoS_2/TiO_2 nanocomposites were classical powder assemblies, difficult for recycling use or requiring additives/binders to prepare the electrodes. It is strongly desirable to easily fabricate TiO_2-film-based nanocomposites with highly defined 1D geometries owing to their advantageous directional charge transfer, improved ion diffusion, and increased active facet exposure. Moreover, the introduction of foreign species with undesirable morphologies is preferentially occurred only at top surface of the TiO_2 NTAs and usually results in the blocking of the tube openings.[40] To the best of our knowledge, a few studies have been reported on the synthesis of MoS_2 nanosheets coating on an array of self-ordered TiO_2 nanotubes nanocomposites.

Herein, a modified two-step anodization approach is proposed to grow highly ordered TiO_2 NTAs with clean top surface, providing easy access for the uniform loading of MoS_2 nanostructures via a facile hydrothermal method. Note that the as-anodized TiO_2 NTAs sample was amorphous and intentionally annealed to anatase in order to increase conductivity before compositing with MoS_2. The oxide film color was found to change from brown to black after the decoration of MoS_2 species. The MoS_2 nanosheets are evenly distributed over the tube top surface and the intertubular voids rather than filling in the tubes, thus allowing these nanotubular channels open to the environment, which are beneficial to efficient transport of ions and electrons. More importantly, these novel TiO_2@MoS_2 nanocomposites exhibit enhanced photocatalytic activity and improved photocurrent response due to the higher light absorption at visible light range and faster charge separation with lower recombination chance comparing to the pristine TiO_2 NTAs. The straightforward and low cost method presented here provides the flexibility of hybridizing 1D self-ordered TiO_2 NTAs with a wide scope of functional semiconducting nanostructures, promising for new opportunities in energy/environment applications, including photocatalysts and other photovoltaic devices.

2. Results and Discussion

The X-ray diffraction (XRD) patterns of the three as-prepared samples: the pristine TiO_2 NTAs, pure MoS_2 sample, and the TiO_2@MoS_2 composites are shown in **Figure 1**. The diffraction patterns for the pristine TiO_2 NTAs match the standard peaks of anatase TiO_2 phase (JCPDS card No. 21-1272) with the lattice parameters of $a = b = 0.316$ nm, $c = 1.230$ nm. A major peak centered at 25.3° can be assigned to (101) facet of anatase TiO_2.[16] As for pure MoS_2 sample, the detected peaks located at 14.2° and 33° can be indexed to (002), (100) planes in the hexagonal phase MoS_2 (JCPDS card No. 37-1492).[27] All diffraction peaks of anatase TiO_2 are still present in the XRD patterns of the TiO_2@MoS_2 composites, suggesting that the intrinsic structure of TiO_2 NTAs are well retained during the hydrothermal reaction. Interestingly, the peak assigned to (002) plane of the MoS_2 (14.2°) is absent. This diffraction peak is corresponding to the *c*-plane of MoS_2 and can be used to study the structure of MoS_2, which is consisted of Mo atoms coordinated with S atoms to form the S–Mo–S sandwiched layer. The absence indicates that the MoS_2 nanosheets decorated on the TiO_2 NTAs may contain only a few layers, too thin to be detected by XRD, indicating that the growth of MoS_2 along the (002) facet might be suppressed by the pure TiO_2 NTAs during the hydrothermal process.[27,41]

Figure 2 depicts the scanning electron microscopy (SEM) images of the structural morphologies of the pure TiO_2 NTAs prepared by a modified two-step anodization method[42,43] from both top surface and cross-sectional views. The anodic TiO_2 NTAs generated by the first anodization exhibits vertically oriented tubular array with an average diameter of ≈60 nm and a film length of ≈9 μm as shown in Figure 2a,b.

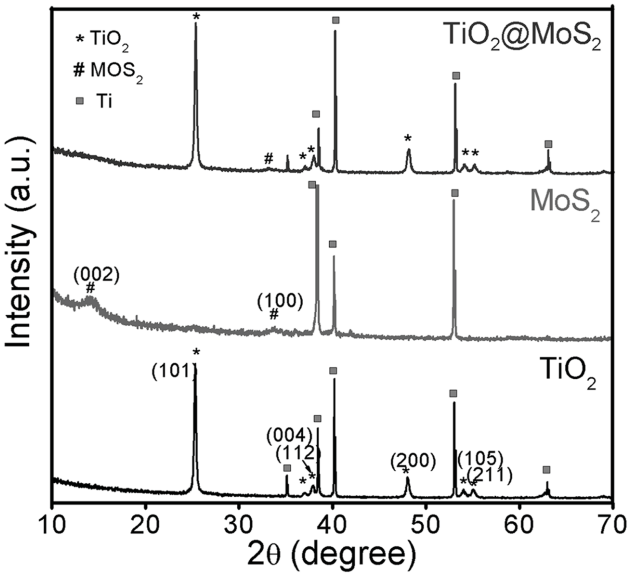

Figure 1. XRD patterns of pristine TiO_2 NTAs, pure MoS_2 sample, and TiO_2@MoS_2 composites.

© 2016 Wiley-VCH Verlag GmbH & Co. KGaA, Weinheim

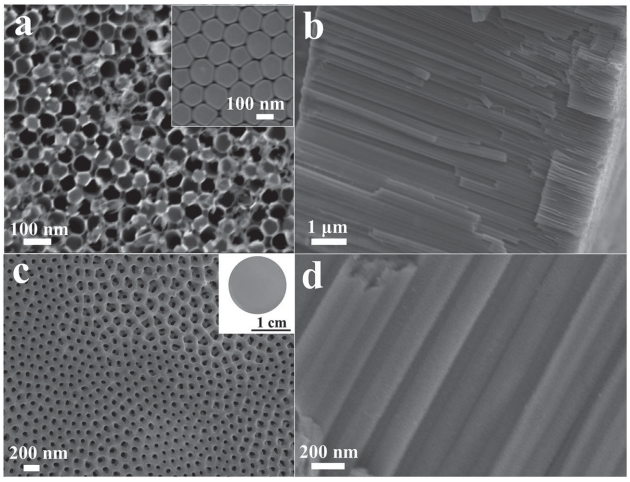

Figure 2. SEM images of the anodized TiO_2 NTAs a,b) at the first time and c,d) the second time, respectively. Inset in (a) shows the bottom view of the TiO_2 NTAs; inset in (c) shows the optical graph of the as-anodized TiO_2 NTAs.

The disordered tube-top structures can be clearly observed, mainly due to the chemical etching upon exposure to fluoride-containing electrolyte which corrodes the upper part of the nanotubes. These undesirable features are detrimental to many applications[43–45] and also easily lead to the random growth of MoS_2. Only a small portion of the MoS_2 nanosheets stack and gather around the tube mouth and randomly decorated on the outer tube walls (Figure S1, Supporting Information). In light of this, a second-anodization process was performed under similar condition to grow highly ordered TiO_2 NTAs with clean top surface as shown in Figure 2c,d with a common brown appearance (inset in Figure 2c). A thin layer of continuous nanoporous structure is formed on the top surface of NTAs with pore diameters ranging from 50 to 170 nm. Noteworthy, these top-porous networks can prevent nanotubes bundling and allow a high tube packing density beneficial to the specific surface area.[43] The average outer tube diameters are estimated to be 140 nm and the overall film thickness is ≈4 μm. It is noted that the clean top surface of the NTAs plays a significant role in providing an easy access for the uniform loading of MoS_2, which will be discussed later.

Typical SEM images of the synthesized TiO_2@MoS_2 composites are illustrated in **Figures 3**a–d and **4**. Distinctly different color (from brown to black, inset in Figure 3a) is readily observed after the decoration of MoS_2 onto TiO_2 NTAs. It is found that with an appropriate loading amount of the MoS_2 precursors, thin MoS_2 nanosheets, interconnected with each other, are evenly distributed on both the tube top surface and the intertubular voids while leaving the tube inside unfilled without obvious morphological change of the TiO_2 NTAs backbones. Additional cross-sectional SEM images were taken from different locations of the TiO_2@MoS_2 composite sample as shown in Figure 4. The results further confirmed the existence of MoS_2 nanosheets decorating in-between the tube gaps. The amount of MoS_2 precursors is critical as they are very likely to aggregate together by forming nanospheres, randomly sitting on top surface of the nanotubes (Figure S2, Supporting Information). As reported,[40,46,47] the introduction of foreign species to the anodic TiO_2 NTAs generally occurs at the top surface and usually blocks the tube openings. In this study, the few-layer MoS_2 nanosheets perfectly decorated around the tube moths and the intertubular gaps, allowing large portion of tube surface accessible to the environment. The reason can be possibly due to higher conductivity of the anatase TiO_2 after thermal annealing treatment

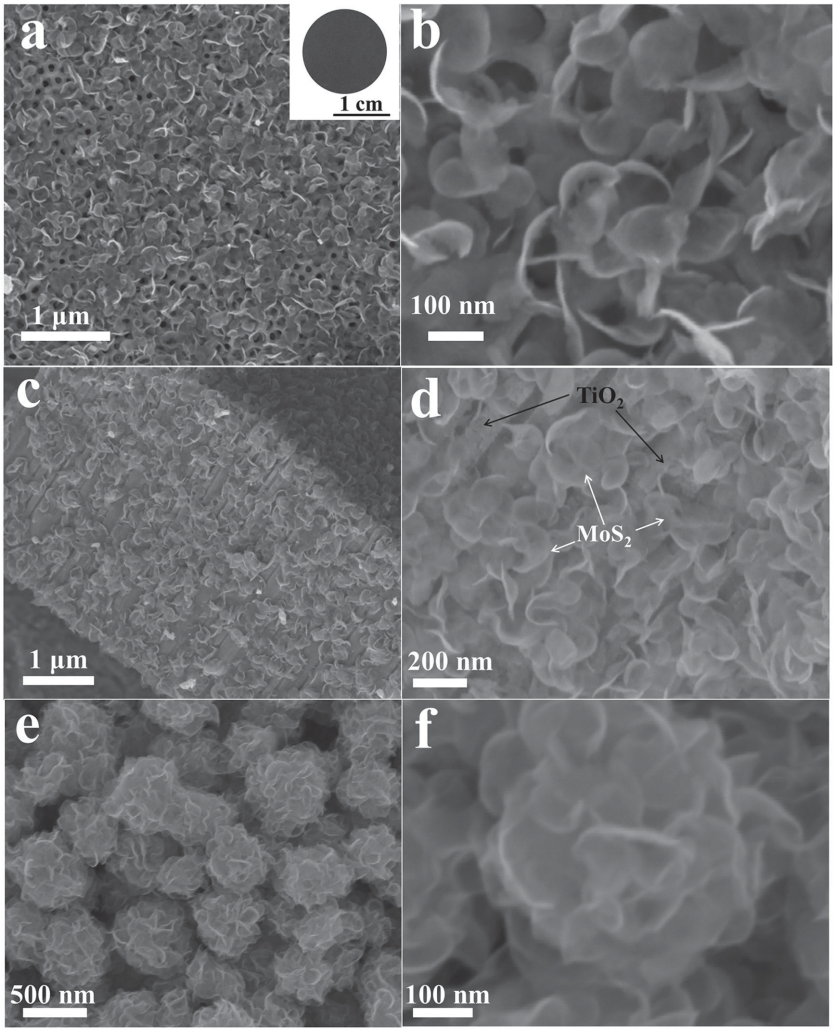

Figure 3. SEM images of TiO_2@MoS_2 composites from both a,b) the top and c,d) the cross-sectional views, and e,f) pure MoS_2 nanospheres. Inset in (a) shows the optical graph of TiO_2@MoS_2 composites.

© 2016 Wiley-VCH Verlag GmbH & Co. KGaA, Weinheim

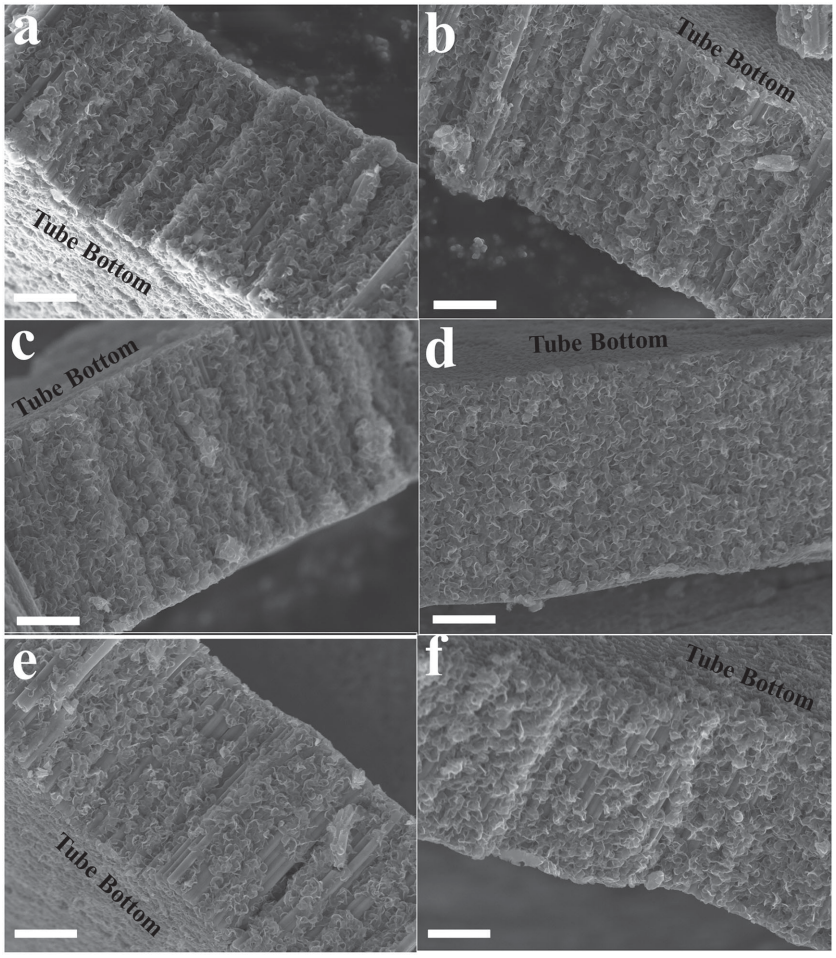

Figure 4. Cross-sectional SEM images of TiO_2@MoS_2 composites taken from different locations of the sample. The scale bar is 1 μm.

than the as-anodized amorphous TiO_2. Confirmed by SEM images in Figure S3 (Supporting Information), due to the semiconductive nature of TiO_2, both MoS_2 nanoparticles and a few nanosheets are formed on the thin continuous porous layer on top of the self-ordered nanotubular array when coupling the MoS_2 with amorphous TiO_2 NTAs.

Thus, clean top surface and crystalline of the anodic TiO_2 NTAs together with the appropriate amount of MoS_2 precursors play a vital role in generating the novel TiO_2@MoS_2 composites. As for pure MoS_2 sample, self-assembly nanospheres (MoS_2 NSs) are formed with diameters ranging from 150 to 500 nm by using the same hydrothermal method without the presence of anodic TiO_2 NTAs (Figure 3e,f).

The morphologies of pristine TiO_2 NTAs and TiO_2@MoS_2 composites were further confirmed by transmission electron microscopy (TEM) and high-resolution TEM (HRTEM) observations (**Figure 5**). As shown in Figure 5a–c, the anodic TiO_2 NTAs are packing closely with diameters ranging from 60 to 160 nm, consistent with the SEM results in Figure 2. The selected area electron diffraction pattern (SAED) (inset of Figure 3c) displays clear anatase diffraction rings consisting of clean diffraction dots, indicating the highly crystalline nature of the pristine TiO_2 NTAs. The well-resolved lattice fringes of 0.35 nm corresponding to the (101) plane of TiO_2 (HRTEM in Figure 5g) also confirm the anatase structure, consistent with the XRD results. The (101) crystallographic plane is determined to be the major exposed surfaces of the NTAs, which is reported to be the most thermodynamically stable crystal facet of anatase TiO_2. Typical low-magnification TEM images of the TiO_2@MoS_2 composites are displayed in Figure 5d–f. Thin MoS_2 nanosheets are coated on the tube top layer and the intertubular gaps, leaving the tube inside unfilled, in agreement with the SEM observations in Figure 3. Due to the high electrical resistivity of native TiO_2, the decoration of foreign species occurs preferentially on top of the layers rather than inside the nanotubes. The distinguished distance of the adjacent lattice fringes with 0.6 nm (Figure 5h–i) can be clearly observed, suggesting the well-defined crystal structure of MoS_2. Moreover, both the readily observed cross lattice fringes and the milky diffraction rings from the SAED (inset in Figure 5f) suggest that the MoS_2 combines the anodic TiO_2 NTAs well to form composite hybrids, promising for photocatalytic activities.

X-ray photoelectron spectroscopy (XPS) analysis was performed to study the chemical components and the states of Mo and S in the TiO_2@MoS_2 nanocomposites. As shown in **Figure 6**a, the survey XPS spectra reveal that the dominant elements are Ti, O, S, Mo, and C of the TiO_2@MoS_2 composites. The high-resolution XPS spectra of Mo, S for pure MoS_2 NSs and TiO_2@MoS_2 composites are indicated in Figure 6b,c. The binding energies of Mo $3d_{3/2}$ and Mo $3d_{5/2}$ for pure MoS_2 nanospheres are ≈232.2 and ≈229.2 eV, respectively, indicating the presence of Mo^{4+}. The separation energy close to 3.0 eV can be ascribed to the typical characteristics of Mo species, which is also existed in the TiO_2@MoS_2 composites with corresponding binding energies of ≈234.2 and ≈229.2 eV, respectively. The high-resolution spectra of S 2p indicate two major peaks at 162.3 eV and 161.1 eV, corresponding to S $2p_{1/2}$ and S $2p_{3/2}$ spin orbits, respectively (Figure 6c). The intensity ratio is ≈1:2 and their separation energy is ≈1.2 eV, in good agreement with previously reported data.[32,48] For the TiO_2@MoS_2 composites, the fitted peaks are shifted to more negative binding energies of ≈1.0 eV, suggesting the electronic interaction between MoS_2 and TiO_2.[32] A comparison of the observed spin-energy separation of ≈5.8 eV between Ti $2p_{1/2}$ and Ti $2p_{3/2}$ peaks indicates a normal chemical state of Ti^{4+} in both pure TiO_2 NTAs and TiO_2@MoS_2 composites (Figure 6d). Similarly, the binding energies of Ti 2p for TiO_2@MoS_2 composites shifted to negative higher energies due to the existence of Ti^{3+} states. As reported,[4] the Ti^{3+} states exhibit higher reactivity by trapping electrons and resulting in the formation of radicals

 © 2016 Wiley-VCH Verlag GmbH & Co. KGaA, Weinheim

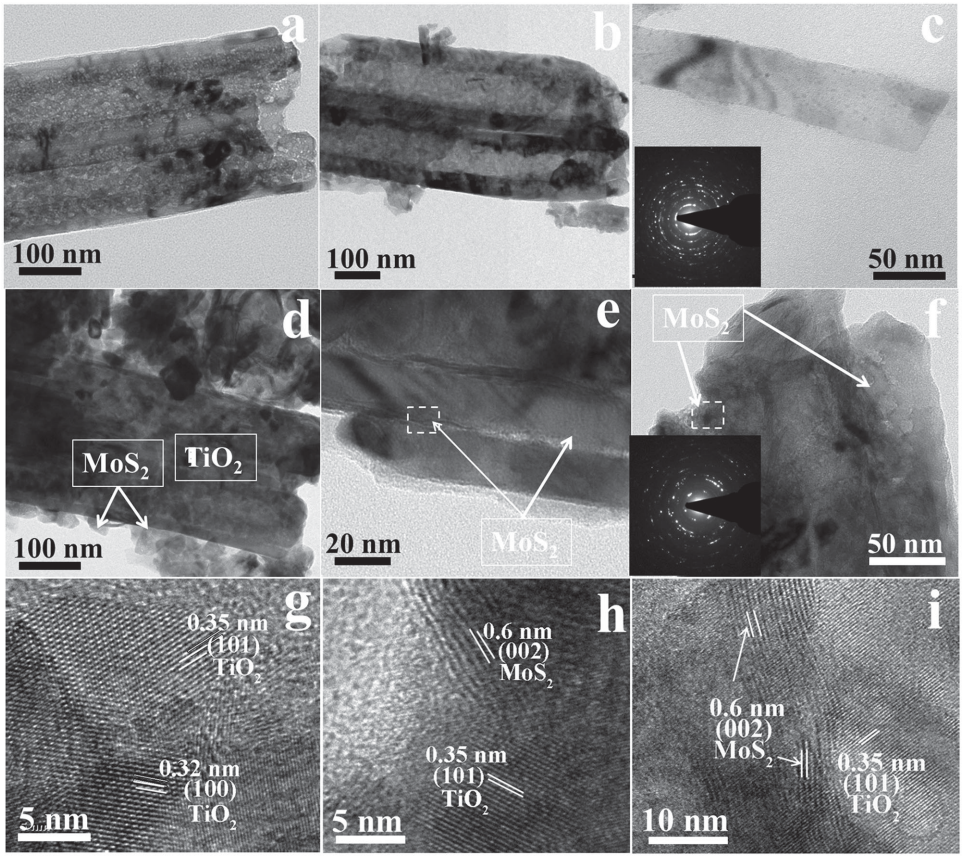

Figure 5. TEM images of a–c) pristine TiO_2 NTAs and d–f) TiO_2@MoS_2 composites. High-resolution TEM (HRTEM) images of g) pristine TiO_2 NTAs and h,i) the designated square parts in (e,f) of TiO_2@MoS_2 composites. Insets in (c,f) show the corresponding SAED patterns.

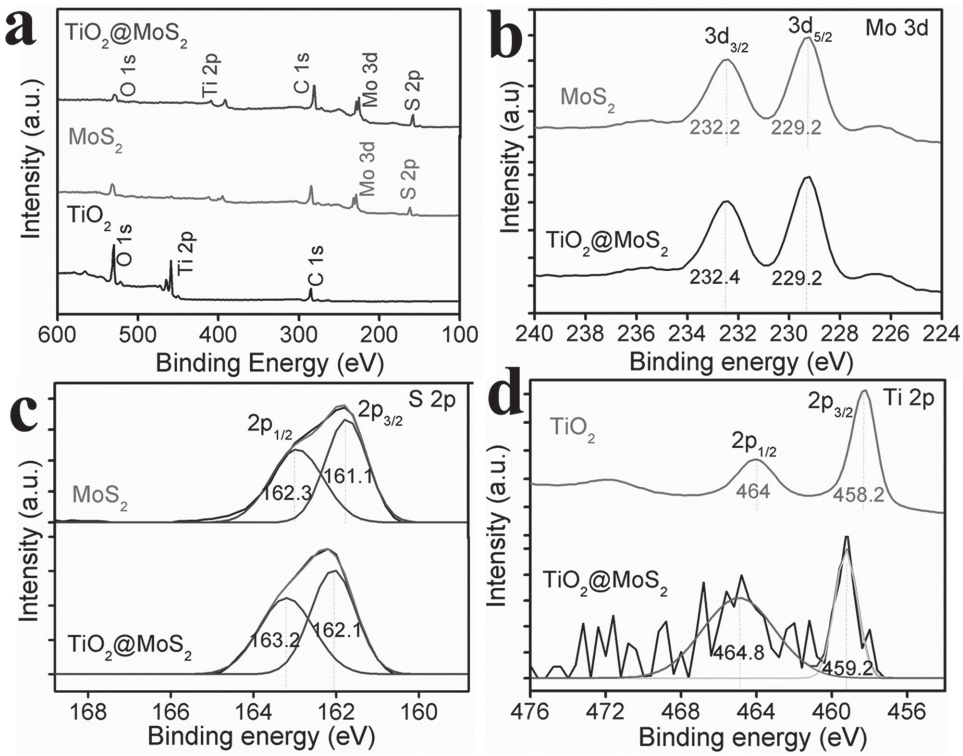

Figure 6. XPS spectra of pristine TiO_2 NTAs, pure MoS_2 NSs, and TiO_2@MoS_2 composites: a) the survey scan, b) Mo 3d, c) S 2p, and d) Ti 2p XPS spectrum.

© 2016 Wiley-VCH Verlag GmbH & Co. KGaA, Weinheim

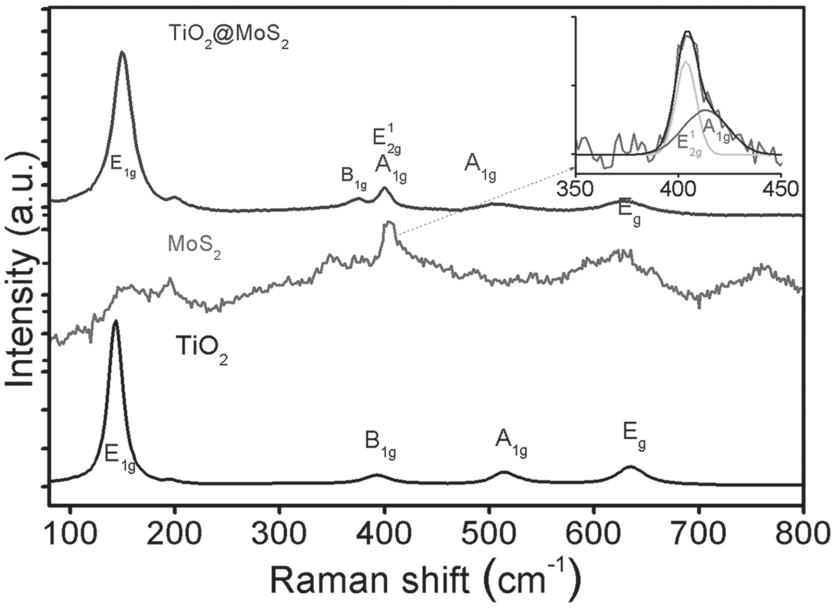

Figure 7. Raman spectra of pristine TiO_2 NTAs, pure MoS_2 NSs, and TiO_2@MoS_2 composites. Inset shows the fitting peaks of the pure MoS_2 sample.

covalently linked to the surface of TiO_2. And these shallow defects can release trapped charge carriers to the nearby conduction or valence bands (VBs) by thermal excitation, beneficial to photocatalytic and photocurrent performances.

Figure 7 shows a comparison of Raman spectra of pristine TiO_2 NTAs, pure MoS_2 NSs, and TiO_2@MoS_2 composites. For TiO_2 NTAs sample, a very intense Raman band with $E_{1g} \approx 145$ cm^{-1} can be observed, corresponding to the main E_g anatase vibration mode. Three strong vibrational peaks located at 392 (B_{1g}), 513 (A_{1g}), and 634 cm^{-1} (E_g) also verify the presence of anatase TiO_2. In the spectrum of pure MoS_2 NSs, a broad peak centred at 403 cm^{-1} is fitted into two dominant scattering peaks (inset in Figure 7) and can be assigned to E_{2g} and A_{1g} modes of MoS_2, respectively. These featuring peaks can also be found in the Raman spectrum of the TiO_2@MoS_2 composites, suggesting the successful introduction of MoS_2 species into the TiO_2 NTAs system. There is a small blue shift observed in the mode of E_{1g}, A_{1g}, and E_g in the TiO_2@MoS_2 composites compared with those of pure TiO_2, which is possibly due to the surface strain induced by the decorated MoS_2 nanosheets on the surface of TiO_2 NTAs.[38,49]

The photocatalytic activity of the unique TiO_2@MoS_2 composite was evaluated by measuring its efficiency in the photodegradation of Rhodamine B (RhB) under UV light (**Figure 8**). RhB is a nonbiodegradable dye commonly used in textile and paper industrials. Before light irradiation, an adsorption–desorption equilibrium would be established between the photocatalysts and RhB in the dark. Interestingly, the TiO_2@MoS_2 composites were found to exhibit stronger adsorption ability toward RhB than both the pristine TiO_2 and pure MoS_2, which was reported to be highly

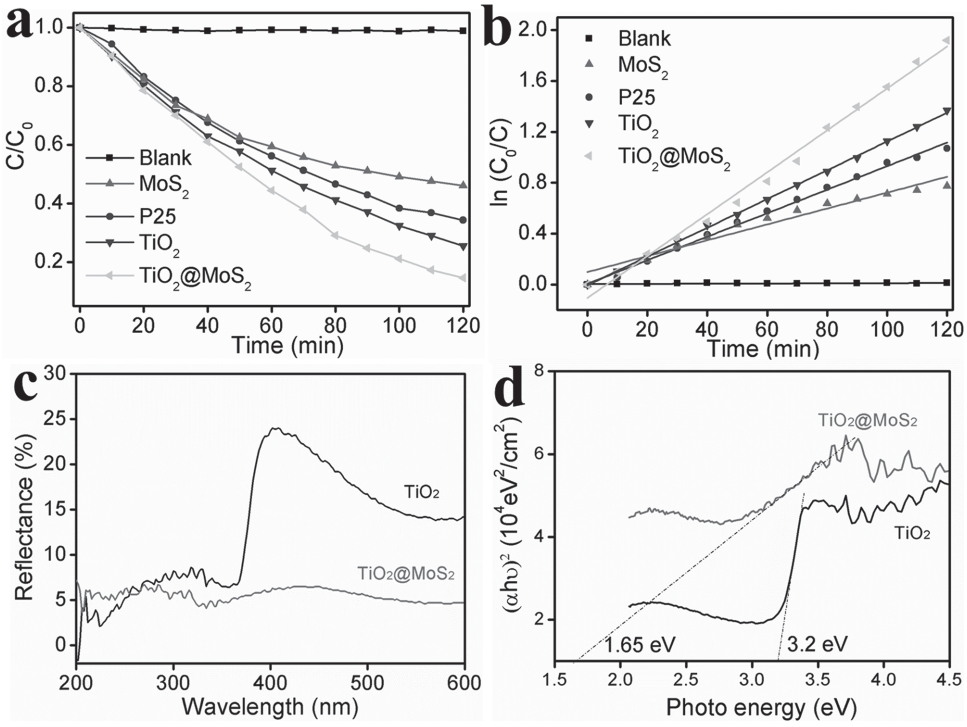

Figure 8. a) The corresponding degradation rate of RhB as a function of irradiation time and b) the plots of $\ln(C_0/C)$ versus time of pure MoS_2 NSs, P25, pristine TiO_2 NTAs, and TiO_2@MoS_2 composites. c) UV–vis diffuse reflectance spectra (DRS) and d) the corresponding plot analysis of optical band gap of pristine TiO_2 NTAs and TiO_2@MoS_2 composites.

© 2016 Wiley-VCH Verlag GmbH & Co. KGaA, Weinheim

favorable to the photocatalytic activity.[27] Control experiment (in the absence of any photocatalysts, denoted as "blank" in Figure 8) reveals that the dye degradation under UV illumination is almost negligible. It is evident that the photodegradation efficiency of the TiO_2@MoS_2 composites is significantly higher than that of pristine TiO_2 NTAs and pure MoS_2 NSs, suggesting the beneficial photocatalytic activity in the composite nanostructures. Notably, comparing to commercially available P25 powder, the efficiency of the TiO_2@MoS_2 composites still proves to be better. To be specific, the concentrations of RhB are reduced by 74.5%, 65.8%, and 53.9% after 120 min of irradiation, respectively, when using the pristine TiO_2 NTAs, P25, and the pure MoS_2 NSs as the photocatalysts. However, the concentration of RhB can be reduced by 85.3% by using the TiO_2@MoS_2 composites. The decomposition of RhB pollutant follows the pseudo-first-order reaction kinetic and can be expressed as: $\ln(C_0/C) = kt$, where C_0 is the initial RhB concentration after adsorption equilibrium, C is the concentration after a certain reaction time, k is the rate constant, and t is the reaction time. In Figure 8b, the k values of pristine TiO_2 NTAs, P25, pure MoS_2 NSs, and TiO_2@MoS_2 composites are calculated to be 0.0113, 0.00925, and 0.00624 min^{-1}, respectively. Evidently, the k value of TiO_2@MoS_2 composites is apparently the highest (0.01646 min^{-1}), which is almost 1.5, 1.8, and 2.6 times higher than that of pure TiO_2 NTAs, P25, and pure MoS_2 NSs, respectively, indicating that the introduction of MoS_2 into TiO_2 can highly promote the enhancement of photocatalytic activity. The photocatalytic activity of semiconductor oxides is known to be mainly governed by light absorption, the recombination rate of photogenerated charge carriers, etc.[50,51] Hence, these factors are discussed as follows.

The optical properties of TiO_2 NTAs and the TiO_2@MoS_2 composites are determined by UV–vis diffuse reflectance spectra (DRS). Comparing with TiO_2 NTAs, the obtained TiO_2@MoS_2 composites exhibit a higher absorption (lower reflectance as shown in Figure 8c) in the visible range (400–600 nm), contributing largely to the enhancement of photocatalytic activity. The energy band gap (E_g) can be estimated by the conventional Tauc equation[40,52]

$$\alpha h\nu = A(h\nu - E_g)^n \quad (1)$$

where $h\nu$ is the photon energy, α is the absorption coefficient, A is the constant, $n = 2$ for an indirectly allowed transition, and $n = 1/2$ for a directly allowed transition. The corresponding Kubelka–Munk transformed reflectance spectra are shown in Figure 8d, where the slopes of the tangents on horizontal axis are band gap energies. The calculated E_g is estimated to be 3.20 eV for pure TiO_2 NTAs (corresponding to the absorption edge of 387 nm) and 1.65 eV for TiO_2@MoS_2 composites (corresponding to the absorption edge of 750 nm), indicating that the presence of MoS_2 enhances the optical absorption properties, which has a positive effect on the photocatalytic activity.

The efficiency of charge trapping and recombination of photoinduced electron-hole pairs in the semiconductor can be verified by the photoluminescence (PL) emission spectrum. As shown in **Figure 9**, the emission spectra of TiO_2@MoS_2 composites appear to be similar with pure TiO_2 NTAs, which means that the loading of MoS_2 nanosheets has not induced new PL. There are three main emission peaks located at 392 nm (≈3.16 eV), 468 nm (≈2.65 eV), and 523 nm (≈2.37 eV). The first peak can be assigned to electronic transition from the bottom of conduction band (CB) to the top of VB, and the other two peaks are likely attributed to the defect levels formed by oxygen vacancies.[53,54] Furthermore, the PL intensity of TiO_2@MoS_2 composites is strongly weakened from 380 to 550 nm than that of the bare TiO_2 NTAs under excitation at 320 nm, suggesting that the recombination of photogenerated electrons and holes is suppressed effectively.[28,51] Therefore, the TiO_2@MoS_2 composite can effectively retard the recombination of photogenerated charge carriers and prolong the lifetime of electron-hole pairs, resulting in the superior photocatalytic activity.

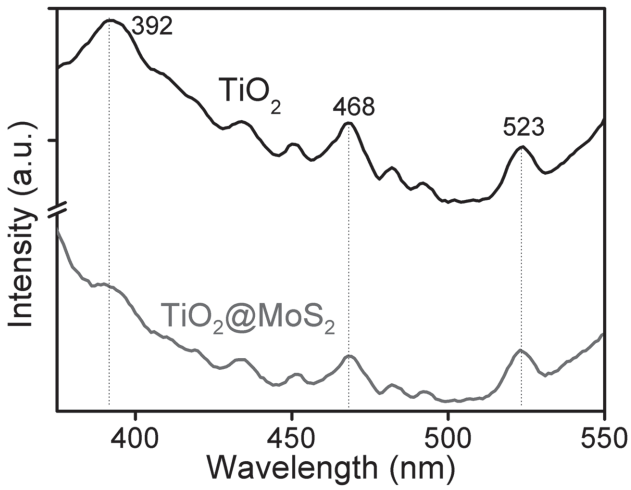

Figure 9. Room temperature PL emission spectra of pristine TiO_2 NTAs and TiO_2@MoS_2 composites with an excitation wavelength of 320 nm.

The heterojunction created between MoS_2 and TiO_2 also exerts great influence on the photocurrent response, as comparatively studied in **Figure 10**. The maximum photocurrent density of TiO_2@MoS_2 composites is ≈7.72 mA cm^{-2}, which is twice higher than that of pristine TiO_2 NTAs (≈3.38 mA cm^{-2}) (Figure 10a), meaning stronger ability of producing charge carriers and more separated electrons in TiO_2@MoS_2 composites. In addition, the onset potential of TiO_2@MoS_2 composites is negatively shifted with respect to pristine TiO_2 NTAs, indicating that more electrons liberated and accumulated in the heterojunction and thus leading to more electronegativity of the anode potential.[55] Figure 10b illustrates the current–time (I–t) characteristics in three different electrodes of pristine TiO_2 NTAs, pure MoS_2 NSs, and TiO_2@MoS_2 composites upon several light ON/OFF cycles. It can be seen that TiO_2@MoS_2 composites display good photoswitching performance with fast response time and stable photostability. The photocurrent density is found to be 3.2 mA cm^{-2}, much higher than that of pristine TiO_2 NTAs (≈2.1 mA cm^{-2}). The photoresponse activity of pure MoS_2 NSs is very low and can be negligible, which is possibly due to the low conductivity of MoS_2 that limits the electron

© 2016 Wiley-VCH Verlag GmbH & Co. KGaA, Weinheim

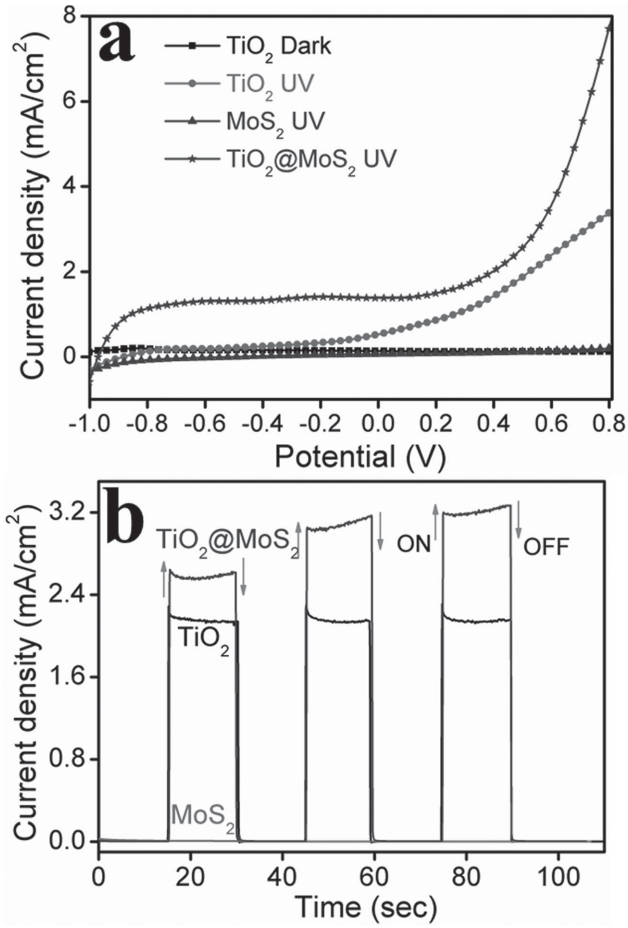

Figure 10. a) Line sweep voltammograms and b) chopped photocurrent response with light ON/OFF every 15 s at an external bias of 0.6 V measured from three different photoelectrodes: pristine TiO_2 NTAs, pure MoS_2 NSs, and TiO_2@MoS_2 composites under Xe lamp illumination.

transfer.[56] The remarkably increased photocurrent density in TiO_2@MoS_2 composites could be ascribed to faster electron transport from VB to CB and a high separation efficiency of the photogenerated electron-hole pairs due to the introduction of MoS_2.

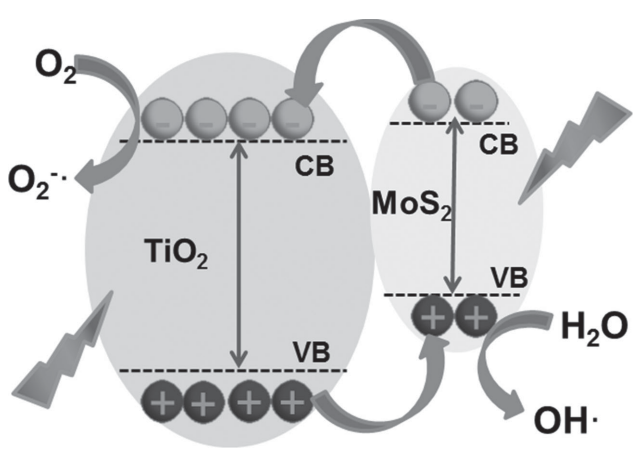

Scheme 1. Schematic illustration of the energy band structure and electron-hole separation of TiO_2@MoS_2 composites.

The Schematic diagram (**Scheme 1**) illustrates the energy band structure and the principle of the separation of charge carriers in TiO_2@MoS_2 composites. In general, anatase TiO_2 has a wide band gap (≈3.2 eV) with a work function of 4.5 eV, while MoS_2 is a narrow band gap (≈1.8 eV) semiconductor with a work function of 4.52 eV.[4,28,57] Upon light illumination, electrons are promptly excited from VB of MoS_2 to CB, leaving behind holes in the VB. Since the CB of TiO_2 is situated lower than that of MoS_2, the TiO_2 can be used as a photoelectronic receiver, and the photo-induced electrons in the CB of MoS_2 could be rapidly transferred to the CB of TiO_2 NTAs.[27,38] The photogenerated electrons can be trapped by oxygen molecules in the aqueous solution to form superoxide radical anions ($O_2 + e^- \rightarrow O_2^-\bullet$), the activated superoxide radical anion $O_2^-\bullet$ could remove organic pollutants or further produces oxygen species via a series of reactions with H^+, such as oxidative H_2O_2, hydroxyl radicals OH•, meanwhile, the holes move in the opposite direction and oxidize water into hydroxyl radicals ($H_2O + h^+ \rightarrow OH\bullet$), which are highly oxidative and can react with organic species to produce mainly carbon dioxide and water. This high interfacial charge transfer and separation ability suppressed the recombination of electron-hole pairs, which explained the enhance photoactivity and improved photocurrent response in TiO_2@MoS_2 composites.[5,53]

3. Conclusions

A novel type of hierarchical TiO_2@MoS_2 composites by decorating thin layer MoS_2 nanosheets onto 1D anodic self-ordered TiO_2 NTAs is successfully prepared by a facile hydrothermal method. The MoS_2 nanosheets are uniformly coated on the tube top surface and the intertubular voids with appearance changing from brown to black color. Anatase TiO_2 NTAs with clean top surface and the appropriate amount of MoS_2 precursors are the keys to grow perfect TiO_2@MoS_2 composites with significantly enhanced photoactivity and improved photocurrent response due to the higher light absorption at visible range and faster charge separation with lower recombination chance comparing to the pristine TiO_2 NTAs. This facile and low-cost method provides the flexibility of hybridizing the self-ordered TiO_2 NTAs with a wide scope of functional semiconducting nanostructures at high throughput rate, and thus would greatly enable the investigation and optimization of the dual-semiconductor material system and accelerating the translation into applications in photocatalysts, and other photovoltaic devices.

4. Experimental Section

Preparation of Anodic TiO_2 NTAs: The titanium foils (0.25 mm thick, 99.7% purity, Sigma-Aldrich) were ultrasonically cleaned in acetone, ethanol, and deionized water successively, and then dried in a nitrogen stream before anodization. Anodic TiO_2 films were generated in a two-electrode electrochemical cell, with a Pt gauze as the counter electrode and a Ti foil as the working

 © 2016 Wiley-VCH Verlag GmbH & Co. KGaA, Weinheim

anode. The Ti working anode was pressed together with an Al foil against an O-ring, defining a working area of 1.766 cm^2 (diameter of 1.5 cm). An anhydrous ethylene glycol (99.8%, Sigma-Aldrich) solution of 0.27 wt% NH_4F (98%+, Sigma-Aldrich) and 5 vol% H_2O was used as the electrolyte. In order to effectively reduce the defects on the surface and help grow well-aligned nanotubular array, the Ti foils were preanodized in the electrolyte at 60 V for 2 h, and then the oxide films were peeled off by ultrasonicating in acetone. Then they were anodized for the second time using fresh electrolyte with the same conditions at 60 V for 20 min to grow the self-ordered NTAs with clean top surface. All the anodization experiments were performed at room temperature. After anodization, the sample was washed with ethanol and then dried in a nitrogen stream. To obtain the anatase TiO_2 NTAs (denoted as pristine TiO_2 NTAs), the as-anodized samples were thermally treated at 450 °C in air for 3 h.

Synthesis of TiO_2@MoS_2 Nanocomposites: Coupling TiO_2 NTAs with MoS_2 nanosheets was achieved by a facile hydrothermal reaction. In a typical process, sodium molybdate dihydrate ($Na_2MoO_4 \cdot 2H_2O$, 10 mg) and thioacetamide (C_2H_5NS, 20 mg) were dissolved in D.I. water (20 mL), stirred for 30 min and then transferred into a 100 mL stainless steel Teflon lined autoclave. The annealed anatase TiO_2 NTAs film was placed at the bottom of the autoclave. The autoclave was put into an electric oven and heated at 200 °C for 24 h, and then cooled to room temperature naturally. The hybrid material was washed several times with distilled water and ethanol, respectively. Finally, the TiO_2@MoS_2 composites were dried in a nitrogen stream. The sample was annealed in an N_2 atmosphere at 450 °C for 2 h to improve the crystallinity of MoS_2. For comparison, pure MoS_2 NSs were synthesized via the similar hydrothermal process using Ti foil as the substrate without the presence of anodic TiO_2 NTAs, and then annealed in N_2 atmosphere at 450 °C for 2 h.

Analysis Instruments: Sample morphologies were characterized using a field emission scanning electron microscopy (FESEM, Model JSM-6701F) and a TEM (Model, TECNAI G^2 S-TWIN). X-ray diffraction patterns were collected on a Bruker D8-A25 diffractometer using Cu Kα radiation (λ = 1.5405 Å). The XPS spectra of the samples were recorded by a Perkin Elmer PHI 5000 C ESCA system equipped with a hemispherical electron energy analyzer, and the Mg Kα (1253.6 eV) anode was operated at 14 kV and 20 mA. The Raman spectroscopy (Spex 403 Raman microscope with 532 nm argon ion laser) was employed to verify chemical bonding characteristics. The optical properties were investigated by optical DRS using a UV–vis spectrophotometer (Hitachi U-4100) with an integrating sphere attachment. PL emission spectra were recorded under ambient conditions (Horiba, Fluoromax-4) with an excitation light at 320 nm induced from an He–Cd laser source.

Photocatalytic Degradation Test: The efficiency of the fabricated films to degrade RhB was measured and used as an indicator of the photocatalytic ability. The tested sample was immersed in an aqueous solution of RhB (5 mL, 10 mg L^{-1}) under UV light (230 W long-wave mercury lamp with main wavelength 365 nm) irradiation at room temperature. The working area of the anodic TiO_2 film was fixed to be 1.766 cm^2 (diameter of 1.5 cm). The mass of the TiO_2 NTAs samples was found to be ≈1 mg by measuring five anatase TiO_2 NTA samples. The control experiments were carried out in absence of any photocatalyst (denoted as "blank"). For comparison, 1 mg P25 powder (Degussa, Germany) was dispersed in 3 mL ethanol, deposited on Ti foil of the same area (1.33 cm × 1.33 cm), followed by a heat treatment at 450 °C for 2 h. The distance between the lamp and the solution was 12 cm. All the tested samples were stirred in the dark for 40 min to achieve the adsorption–desorption equilibrium between RhB and the photocatalysts. The concentration of RhB was monitored as a function of reaction time using a UV–vis spectrometer (Hitachi U-4100). The concentration of RhB was calculated from the absorption maxima located at 554 nm.

Photoelectrochemical Measurements: Photocurrent measurements were performed on an electrochemical workstation (CHI 660E, Chenhua, Shanghai) in a standard three-electrode configuration with three different photoelectrodes: pristine TiO_2 NTAs, pure MoS_2 NSs, and TiO_2@MoS_2 composites, as the working electrodes. All the samples can be used directly as electrodes under front illumination with back sides of the substrates covering with tape. The counter electrode and the reference electrode were Pt sheet and Ag/AgCl electrode, respectively. Time-dependent photoresponse tests were carried out by measuring the photocurrent under chopped light irradiation (light/dark cycles of 15 s) at a fixed bias of 0.6 V versus Ag/AgCl. A 0.1 M Na_2SO_4 aqueous solution was used as the electrolyte. The working area used was fixed at 1.766 cm^2 (diameter of 1.5 cm). The working electrode was irradiated by Xe lamp during the measurements. The distance between the working electrode and the light source was 20 cm and the focused incident light intensity on the working electrode was ≈80 mW cm^{-2}.

Supporting Information

Supporting Information is available from the Wiley Online Library or from the author.

Acknowledgements

This work was supported by the Science and Technology Commission of Shanghai Municipality (15520720700 and 13NM1400300), the National Natural Science Foundation of China (Grant No. 51471051), the Shanghai Shu Guang Project (12SG01), and the Programs for Professor of Special Appointment (Eastern Scholar) at Shanghai Institutions of Higher Learning. Part of the experimental work was carried out in Fudan Nanofabrication Laboratory.

[1] A. Fujishima, K. Honda, *Nature* **1972**, *238*, 37.
[2] R. Asahi, T. Morikawa, T. Ohwaki, K. Aoki, Y. Taga, *Science* **2001**, *293*, 269.
[3] S. U. M. Khan, M. Al-Shahry, W. B. Ingler, *Science* **2002**, *297*, 2243.
[4] P. Roy, S. Berger, P. Schmuki, *Angew. Chem. Int. Ed.* **2011**, *50*, 2904.
[5] J. Schneider, M. Matsuoka, M. Takeuchi, J. Zhang, Y. Horiuchi, M. Anpo, D. W. Bahnemann, *Chem. Rev.* **2014**, *114*, 9919.

© 2016 Wiley-VCH Verlag GmbH & Co. KGaA, Weinheim

[6] H. A. Hamedani, N. K. Allam, M. A. El-Sayed, M. A. Khaleel, H. Garmestani, F. M. Alamgir, *Adv. Funct. Mater.* **2014**, *24*, 6783.
[7] S. G. Kumar, L. G. Devi, *J. Phys. Chem. A* **2011**, *115*, 13211.
[8] K. Lee, A. Mazare, P. Schmuki, *Chem. Rev.* **2014**, *114*, 9385.
[9] A. Ghicov, P. Schmuki, *Chem. Commun.* **2009**, 2791.
[10] V. M. Prida, E. Manova, V. Vega, M. Hernandez-Velez, P. Aranda, K. R. Pirota, M. Vázquez, E. Ruiz-Hitzky, *J. Magn. Magn. Mater.* **2007**, *316*, 110.
[11] M. Favaro, S. Leonardi, C. Valero-Vidal, S. Nappini, M. Hanzlik, S. Agnoli, J. Kunze-Liebhäuser, G. Granozzi, *Adv. Mater. Interfaces* **2015**, *2*, 1400462.
[12] A. El Ruby Mohamed, S. Rohani, *Energy Environ. Sci.* **2011**, *4*, 1065.
[13] H. Li, Z. Chen, C. K. Tsang, Z. Li, X. Ran, C. Lee, B. Nie, L. Zheng, T. Hung, J. Lu, B. Pan, Y. Y. Li, *J. Mater. Chem. A* **2014**, *2*, 229.
[14] V. M. Prida, M. Hernández-Vélez, K. R. Pirota, A. Menéndez, M. Vázquez, *Nanotechnology* **2005**, *16*, 2696.
[15] I. M. Low, H. Albetran, V. M. Prida, V. Vega, P. Manurung, M. Ionescu, *J. Mater. Res.* **2013**, *28*, 304.
[16] C. W. Kim, S. P. Suh, M. J. Choi, Y. S. Kang, Y. S. Kang, *J. Mater. Chem. A* **2013**, *1*, 11820.
[17] J. Zhang, J. H. Bang, C. Tang, P. V. Kamat, *ACS Nano* **2010**, *4*, 387.
[18] K. Xie, Q. Wu, Y. Wang, W. Guo, M. Wang, L. Sun, C. Lin, *Electrochem. Commun.* **2011**, *13*, 1469.
[19] Q. Zhang, H. Xu, W. Yan, *Electrochim. Acta* **2012**, *61*, 64.
[20] K.-K. L. Dung-Sheng Tsai, D. H. Lien, M. L. Tsai, C. F. Kang, C. A. Lin, L. J. Li, J. H. He, *ACS Nano* **2013**, *7*, 3905.
[21] M. R. Esmaeili-Rad, S. Salahuddin, *Sci. Rep.* **2013**, *3*, 2345.
[22] O. Lopez-Sanchez, D. Lembke, M. Kayci, A. Radenovic, A. Kis, *Nat. Nanotechnol.* **2013**, *8*, 497.
[23] G. Ma, H. Peng, J. Mu, H. Huang, X. Zhou, Z. Lei, *J. Power Sources* **2013**, *229*, 72.
[24] J. Li, X. Liu, L. Pan, W. Qin, T. Chen, Z. Sun, *RSC Adv.* **2014**, *4*, 9647.
[25] Y. Yang, H. Fei, G. Ruan, C. Xiang, J. M. Tour, *Adv. Mater.* **2014**, *26*, 8163.
[26] Y. Yan, B. Xia, N. Li, Z. Xu, A. Fisher, X. Wang, *J. Mater. Chem. A* **2015**, *3*, 131.
[27] W. Zhou, Z. Yin, Y. Du, X. Huang, Z. Zeng, Z. Fan, H. Liu, J. Wang, H. Zhang, *Small* **2013**, *9*, 140.
[28] Y. Liu, Y. X. Yu, W. D. Zhang, *J. Phys. Chem. C* **2013**, *117*, 12949.
[29] Z. Chen, D. Cummins, B. N. Reinecke, E. Clark, M. K. Sunkara, T. F. Jaramillo, *Nano Lett.* **2011**, *11*, 4168.
[30] J. Li, K. Yu, Y. Tan, H. Fu, Q. Zhang, W. Cong, C. Song, H. Yin, Z. Zhu, *Dalton Trans.* **2014**, *43*, 13136.
[31] X. Li, W. Li, M. Li, P. Cui, D. Chen, T. Gengenbach, L. Chu, H. Liu, G. Song, *J. Mater. Chem. A* **2015**, *3*, 2762.
[32] C. Liu, L. Wang, Y. Tang, S. Luo, Y. Liu, S. Zhang, Y. Zeng, Y. Xu, *Appl. Catal. B: Environ.* **2015**, *164*, 1.
[33] H. Liu, T. Lv, C. Zhu, X. Su, Z. Zhu, *J. Mol. Catal. A: Chem.* **2015**, *396*, 136.
[34] X. Zhu, C. Yang, F. Xiao, J. Wang, X. Su, *New J. Chem.* **2015**, *39*, 683.
[35] W. Zhuang, L. Li, J. Zhu, R. An, L. Lu, X. Lu, X. Wu, H. Ying, *ChemElectroChem* **2015**, *2*, 374.
[36] H. Fu, K. Yu, H. Li, J. Li, B. Guo, Y. Tan, C. Song, Z. Zhu, *Dalton Trans.* **2015**, *44*, 1664.
[37] B. Guo, K. Yu, H. Fu, Q. Hua, R. Qi, H. Li, H. Song, S. Guo, Z. Zhu, *J. Mater. Chem. A* **2015**, *3*, 6392.
[38] M. Shen, Z. Yan, L. Yang, P. Du, J. Zhang, B. Xiang, *Chem. Commun.* **2014**, *50*, 15447.
[39] X. Xu, Z. Fan, S. Ding, D. Yu, Y. Du, *Nanoscale* **2014**, *6*, 5245.
[40] P. Li, H. Hu, J. Xu, H. Jing, H. Peng, J. Lu, C. Wu, S. Ai, *Appl. Catal. B: Environ.* **2014**, *147*, 912.
[41] K. Chang, W. Chen, *J. Mater. Chem.* **2011**, *21*, 17175.
[42] S. P. Albu, P. Schmuki, *Phys. Status Solidi-RRL* **2010**, *4*, 151.
[43] D. Wang, Y. Liu, C. Wang, F. Zhou, W. Liu, *ACS Nano* **2009**, *3*, 1249.
[44] D. Kim, A. Ghicov, P. Schmuki, *Electrochem. Commun.* **2008**, *10*, 1835.
[45] M. Ye, X. Xin, C. Lin, Z. Lin, *Nano Lett.* **2011**, *11*, 3214.
[46] N. A. Kyeremateng, C. Lebouin, P. Knauth, T. Djenizian, *Electrochim. Acta* **2013**, *88*, 814.
[47] N. Liu, K. Lee, P. Schmuki, *Angew. Chem. Int. Ed.* **2013**, *52*, 12381.
[48] T. L. Hui Liu, Chunkui Zhu, Xing Su, Zhenfeng Zhu, *J. Mol. Catal. A: Chem.* **2015**, *396*, 136.
[49] C. Y. Xu, P. X. Zhang, L. Yan, *J. Raman Spectrosc.* **2001**, *32*, 862.
[50] L.-W. Zhang, H.-B. Fu, Y.-F. Zhu, *Adv. Funct. Mater.* **2008**, *18*, 2180.
[51] S. C. Han, L. F. Hu, Z. Q. Liang, S. Wageh, A. A. Al-Ghamdi, Y. S. Chen, X. S. Fang, *Adv. Funct. Mater.* **2014**, *24*, 5719.
[52] Y. Wang, Y. N. Zhang, G. Zhao, H. Tian, H. Shi, T. Zhou, *ACS Appl. Mater. Interfaces* **2012**, *4*, 3965.
[53] C. C. Mercado, F. J. Knorr, J. L. McHale, *ACS Nano* **2012**, *6*, 7270.
[54] F. Teng, G. Zhang, Y. Wang, C. Gao, L. Chen, P. Zhang, Z. Zhang, E. Xie, *Appl. Surf. Sci.* **2014**, *320*, 703.
[55] Q. Liu, H. Lu, Z. Shi, F. Wu, J. Guo, K. Deng, L. Li, *ACS Appl. Mater. Interfaces* **2014**, *6*, 17200.
[56] N. Zhang, S. Gan, T. Wu, W. Ma, D. Han, L. Niu, *ACS Appl. Mater. Interfaces* **2015**, *7*, 12193.
[57] E. Scalise, M. Houssa, G. Pourtois, V. V. Afanas'ev, A. Stesmans, *Physica E* **2014**, *56*, 416.

Received: November 11, 2015
Revised: December 14, 2015
Published online: January 22, 2016

© 2016 Wiley-VCH Verlag GmbH & Co. KGaA, Weinheim